

Ab-initio perspective on structural and electronic properties of iron-based superconductors

Daniel Guterding, Steffen Backes, Milan Tomić, Harald O. Jeschke, and Roser Valentí

*Institut für Theoretische Physik, Goethe-Universität Frankfurt,
Max-von-Laue-Straße 1, 60438 Frankfurt am Main, Germany*

The discovery of iron pnictides and iron chalcogenides as a new class of unconventional superconductors in 2008 has generated an enormous amount of experimental and theoretical work that identifies these materials as correlated metals with multiorbital physics, where magnetism, nematicity and superconductivity are competing phases that appear as a function of pressure and doping. A microscopic understanding of the appearance of these phases is crucial in order to determine the nature of superconductivity in these systems. Here we review our recent theoretical efforts to describe and understand from first principles the properties of iron pnictides and chalcogenides with special focus on (i) pressure dependence, (ii) effects of electronic correlation and (iii) origin of magnetism and superconductivity.

1. INTRODUCTION

The discovery of iron-based superconductivity in $\text{LaFeAsO}_{1-x}\text{F}_x$ with a $T_c = 26 \text{ K}^1$ created a new field of research and incited intense experimental and theoretical work in this area. Here we review our present theoretical knowledge of the microscopic behavior of these materials. In particular, we elucidate via first principles investigations the influence of pressure, correlations and, to a less extent, doping on the electronic, magnetic and superconductor properties of these materials. For our analysis we consider a combination of density functional theory (DFT), dynamical mean-field theory (DMFT) and spin fluctuation theory.

Crystal structure.- The basic building block of all iron-based superconductors is a two-dimensional square lattice of iron atoms, tetrahedrally coordinated by pnictogen or chalcogen atoms (Fig. 1). The resulting structure is a tri-layer, where the iron layer is sandwiched between two layers of pnictogen or chalcogen atoms. The C_4 symmetry of the iron lattice translates into the tetragonal symmetry of the overall crystal lattice, unless broken by

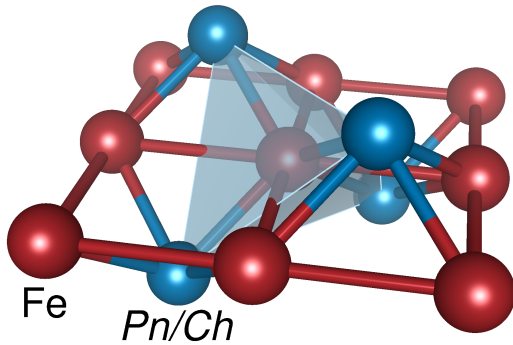


FIG. 1: Structural building block of iron pnictide and chalcogenide superconductors. *Pn* stands for the pnictogen phosphorous or arsenic, *Ch* for the chalcogen sulphur, selenium or tellurium.

magnetic ordering. Trilayers can be stacked in different fashions. Between layers, there can be (i) no ions (FeSe as representative of the 11 family of chalcogenides), (ii) alkali ions (LiFeAs as typical member of the so called 111 family of pnictides), (iii) alkaline earth ions (CaFe_2As_2 is the lightest representative of the 122 family), (iv) rare earth oxides (LaFeAsO as prototype of the 1111 family) and (v) even perovskites and organic molecules. The crystal structure of the various families is referred to by the stoichiometry of the corresponding formula unit. In this review we consider iron-based superconductors with unit cells containing either one or two tri-layers. We especially focus on the 122 family with two trilayers in the unit cell, which belongs to the ThCr_2Si_2 crystal structure type². A well known instability of these structures is a collapse along the crystallographic *c*-axis, when bonds are formed between the pnictogen sublayers of adjacent trilayers.

Electronic structure and pressure effects.- Iron-based superconductors are *3d* metals with iron in a nominal +2 oxidation state (Fe $3d^6$). In the (imperfect) tetrahedral environment of pnictogen/chalcogen, iron *3d* orbitals hybridize with the pnictogen/chalcogen *p* orbitals and split approximately into the doubly degenerate e_g and triply degenerate t_{2g} orbitals. The physics of iron-based superconductors is fundamentally multi-orbital involving all five *3d* orbitals and to a lesser extent the pnictogen/chalcogen *p* orbitals. The physics at the Fermi level is dominated by the t_{2g} orbitals, with a subdominant role played by e_g and *p* orbitals.

When pressure is applied to these systems, it couples to bond lengths and angles, forcing new equilibrium positions of all atoms within a changed unit cell. Therefore, pressure is a very direct way of modifying the crystal structure, electronic properties and magnetism³. The 122 family of iron pnictides has been the focus of many experimental and theoretical pressure studies. Of particular interest are CaFe_2As_2 , where As *p*-As *p* bonds form easily along *c* and lead to a structural collapse, and BaFe_2As_2 , where the larger Ba atom suppresses inter-

layer bonding. At ambient pressure and a temperature of 172 K, CaFe_2As_2 undergoes a sharp first order transition from the paramagnetic tetragonal phase into the orthorhombic antiferromagnetically ordered phase⁴⁻⁹. This transition can be suppressed by the application of pressure^{8,10-14} and the paramagnetic collapsed tetragonal phase can be observed at around 0.4 GPa. These systems show high sensitivity to the hydrostaticity of the applied pressure^{8,10,15,16}. Interestingly, under good hydrostatic conditions CaFe_2As_2 does not show any signal of superconductivity¹⁰, which is however the case when a non-hydrostatic component is present. In addition, application of purely uniaxial pressure along the crystallographic c -axis reduces the pressure at which the collapsed tetragonal occurs by an order of magnitude to 0.06 GPa¹⁵.

BaFe_2As_2 undergoes a transition from the tetragonal paramagnetic into the orthorhombic antiferromagnetic phase at ambient pressure and a temperature of 140 K¹⁷. Application of pressure within a certain range produces a superconducting dome¹⁸⁻²⁰, beyond which magnetic order is suppressed and a tetragonal phase emerges, followed by the collapsed tetragonal phase at even higher pressures^{21,22}. The situation in BaFe_2As_2 is complicated by phase coexistence. The tetragonal signature can be observed already at 6 GPa by neutron diffraction²³ although BaFe_2As_2 stays magnetically ordered up to 10 GPa²². Sensitivity to non-hydrostaticity along the c -axis has been also reported²¹.

Various strain conditions on the ab -plane have been also investigated and are presently still a subject of intensive discussion. Experimentally, in-plane application of tensile strain is used to detwin samples²⁴⁻³⁰ in order to provide a better insight into the anisotropic properties, in particular, in relation to the so-called nematic phase³¹⁻³³. In addition, it has been shown that in-plane strain has a significant impact on the magnetic properties of BaFe_2As_2 ^{28,34}. In section 3 we present our simulations on pressure effects in the 122 systems.

Correlation effects. - An important aspect of iron-based superconductors is the role of electronic correlations in determining the behavior of these systems. The investigation of correlation effects in these materials has been a subject of intensive research since their discovery. The observation of significant band renormalizations and mass enhancements in optical spectroscopy³⁵, photoemission spectroscopy³⁶⁻³⁸ and quantum oscillation experiments³⁹⁻⁴³ or the detection of an incoherent bad metal to coherent Fermi liquid phase transition at low temperatures^{44,45} are experimental examples that clearly set these systems as correlated metals. However, the true nature of these materials is still a subject of debate; namely whether these materials are on the verge of being Mott insulators or, alternatively, they behave as Hund's metals.

While the metallic nature of these materials has made a DFT-based description enormously successful⁴⁶, there are many aspects which are less well captured within

DFT like band renormalizations and mass enhancements: DFT bands and Fermi surfaces differ quantitatively and sometimes qualitatively from experimental observations. Also, the absence of quantum fluctuations in the magnetic DFT description has some serious consequences. Therefore, an improved treatment of electronic correlations has been discussed to be important for quantitative comparisons with experiment.

A method that has proven quite successful in capturing the essential features of electronic correlations in iron-based superconductors is the combination of density functional theory with dynamical mean-field theory (DFT+DMFT)⁴⁷⁻⁵³. It treats both itinerant and localized properties of the electrons on equal footing. Many studies have dealt with the experimentally observed effects of correlation like large masses enhancements or possible non-Fermi liquid behavior^{47,48,51,52,54-56}. The physics of iron-based superconductors is controlled by all Fe $3d$ orbitals, leading to a multiple orbital problem crucially influenced by the Hund's coupling J_H ^{51,52,54-59}. However, the relative importance and the role of J_H versus the on-site Coulomb repulsion U is an ongoing debate in the interpretation of the correlated nature of Fe-pnictides and Fe-chalcogenides^{47,54,55,59-63}. An important insight has been gained in several studies by recognizing that depending on the electronic filling, the Hund's coupling J_H can, on the one hand, render a moderately correlated system even more correlated and push it into a bad metal regime, while, on the other hand, it can also reestablish a metallic behavior, albeit orbital selective, in a strongly correlated system^{59,63}.

For the investigation of typical correlation effects such as band and effective mass renormalizations, as well as Hubbard satellites, in section 4 we review LiFeAs , LiFeP , LaFePO , CaFe_2As_2 and the hole-doped $A\text{Fe}_2\text{As}_2$ ($A = \text{K}, \text{Rb}, \text{Cs}$) end members of the 122 iron pnictide series in order to allow a comparative analysis of different degrees of correlation and their consequences on the properties of Fe-based superconductors. The latter family of systems is ideal for investigating the effects of correlation versus *negative* pressure, as the unit cell expands along the series. The removal of one electron per formula unit by substitution of Ba by K in BaFe_2As_2 is accompanied by a complete suppression of any structural or magnetic phase transition^{20,45} and by the emergence of superconductivity at low temperatures⁶⁴. This behavior is quite generic in all hole-doped end members $A\text{Fe}_2\text{As}_2$ ⁶⁵⁻⁶⁹.

There is also experimental evidence that the parent compound $\text{Ba}_{1-x}\text{K}_x\text{Fe}_2\text{As}_2$ undergoes a coherence-incoherence transition^{44,53,70} as a function of temperature, probably caused by a strong increase in correlations, since the system is pushed closer to half filling^{40,71,72}. Experimental determination of the Sommerfeld coefficient seems to indicate that these hole-doped end systems are one the most strongly correlated known 122 iron-pnictide superconductors^{44,67}, which is also indicated by multiple theoretical investigations on KFe_2As_2 ^{44,47,62,73}. Along the doping series from BaFe_2As_2 to KFe_2As_2 the Som-

merfeld coefficient increases by more than an order of magnitude^{44,45,74} and further continues to increase as K is substituted by atoms with larger atomic radius like the isovalent Rb and Cs^{68,75}.

Superconductivity.- It was realized early on that superconductivity in iron-based materials is unconventional and probably mediated by spin-fluctuations⁷⁶. Although this is not ultimately settled, research in this area has become relatively mature and a number of reviews on the topic have appeared^{77–81}. It is widely believed that the strong orbital differentiation and almost two-dimensional electronic structure are the key features of iron-based superconductors. The questions remaining to be answered are (i) whether a unified model of iron-based superconductors exists and (ii) how the superconducting transition temperature can be optimized. In section 5 we discuss our present understanding of superconductivity by reviewing the superconducting behavior of a few families of iron-based superconductors.

2. METHODS

Our investigations are based on first principles calculations combining density functional theory, dynamical mean-field theory and spin fluctuation theory. In this section we present the details of the three approaches.

DFT calculations.- For the density functional theory calculations we use the all-electron full-potential local orbital (FPLO)⁸² code in the generalized gradient approximation (GGA)⁸³, as well as the WIEN2K⁸⁴ implementation of the full-potential linear augmented plane wave (FLAPW) method in both GGA and the local density approximation (LDA) and we also employed the Vienna ab initio simulations package (VASP)^{85,86} with the projector augmented wave (PAW) basis⁸⁷. All of our structural relaxations presented were performed under constant stress using the Fast Inertial Relaxation Engine (FIRE)⁸⁸, with a modified relaxation algorithm⁸⁹.

LDA+DMFT calculations.- We combine the DFT method with dynamical mean-field theory (DMFT) to include electronic correlation effects beyond the local density approximation. In the DMFT approximation one assumes that the coordination number Z (number of nearest neighbours) is large, so that non-local fluctuations are small because they tend to be averaged out for large Z . As has been shown^{90,91}, in the limit of $Z \rightarrow \infty$, this approximation is exact and the self-energy becomes a local quantity

$$\Sigma_{ij}(\omega) \rightarrow \delta_{ij} \Sigma_{ii}(\omega), \quad (1)$$

where i, j label the atomic sites, and correspondingly, its Fourier transform is momentum independent. In this limit, the self-energy can be obtained by a self-consistent solution of an effective Anderson impurity model⁹². With this, the interacting Green's function can be written as

$$G(k, \omega) = [\omega + i\delta + \mu - \epsilon_k - \Sigma(\omega)]^{-1}, \quad (2)$$

where $\delta > 0$ is a small convergence parameter. The dispersion ϵ_k is given by the non-interacting system, which is approximately given (minus a doublecounting term) by the DFT result.

We implemented our own version of the LDA+DMFT cycle (see Ref. 93 for a more detailed explanation), in combination with the continuous-time quantum Monte Carlo method in the hybridization expansion⁹⁴ as implemented in the ALPS^{95,96} project for solving the effective impurity model. For the DFT calculations we used the WIEN2K⁸⁴ implementation of the FLAPW method in the local density approximation. A local orbital basis was obtained by a projection of the Bloch wave functions to the localized Fe $3d$ orbitals, using our implementation of the projection described in Refs. 57,97. The interaction parameters were used in the definition of the Slater integrals⁹⁸ F^k with $U = F^0$ and $J_H = (F^2 + F^4)/14$. Observables like the effective masses can be directly calculated from the impurity self-energy via

$$\frac{m^*}{m_{\text{LDA}}} = 1 - \left. \frac{\partial \text{Im}\Sigma(i\omega)}{\partial i\omega} \right|_{\omega \rightarrow 0^+}, \quad (3)$$

with $i\omega$ on the Matsubara axis. The continuation of the Monte Carlo data to the real axis was done by stochastic analytic continuation⁹⁹.

RPA spin-fluctuation calculations.- Soon after the discovery of iron-based superconductors it was suggested that superconductivity in these materials might be unconventional and mediated by antiferromagnetic spin-fluctuations⁷⁶. Subsequently, several groups developed methods of calculating the symmetry of the superconducting order parameter and the pairing strength based on the electronic bandstructure and an interaction term (for a review see Ref. 77). One of those methods is the random phase approximation (RPA) approach to the multi-orbital Hubbard model^{100,101}, which we briefly review here.

In this method, the Hamiltonian consists of a kinetic part H_0 and an interaction term H_{int} . The kinetic part is usually a Wannier representation of the DFT bandstructure. The crystallographic unit cell contains two iron atoms, contributing 2×5 d -orbitals close to the Fermi level, and two pnictogen or chalcogen atoms, contributing 2×3 p -orbitals close to the Fermi level. In consequence, a good representation of the DFT bands can be obtained with a 16-orbital tight binding model. Such a model of the two-iron Brillouin zone can be approximately unfolded to an 8-orbital model of the effective one-iron Brillouin zone by using the glide reflection symmetry of the unit cell. To handle this we have developed a generalized unfolding method relying on induced representations of space groups¹⁰². For the interaction term H_{int} the multi-orbital Hubbard interaction is used on the iron site. Here, σ represents the spin, $n_{i\sigma} = c_{i\sigma}^\dagger c_{i\sigma}$ and

$n_{il} = n_{il\uparrow} + n_{il\downarrow}$. The indices l denote the atomic orbitals.

$$\begin{aligned}
H &= H_0 + H_{\text{int}} \\
&= \sum_{l_1, l_2 \sigma} \sum_{\langle ij \rangle} t_{ij}^{l_1 l_2} c_{il_1 \sigma}^\dagger c_{jl_2 \sigma} + U \sum_{i, l} n_{il\uparrow} n_{il\downarrow} \\
&\quad + \frac{V}{2} \sum_{i, l_1, l_2 \neq l_1} n_{il_1} n_{il_2} - \frac{J}{2} \sum_{i, l_1, l_2 \neq l_1} \vec{S}_{il_1} \cdot \vec{S}_{il_2} \quad (4) \\
&\quad + \frac{J'}{2} \sum_{i, l_1, l_2 \neq l_1, \sigma} c_{il_1 \sigma}^\dagger c_{il_1 \bar{\sigma}}^\dagger c_{il_2 \bar{\sigma}} c_{il_2 \sigma}
\end{aligned}$$

Subsequently, the non-interacting static susceptibility χ^0 is calculated,

$$\begin{aligned}
\chi_{l_1 l_2 l_3 l_4}^0(\vec{q}) &= -\frac{1}{N} \sum_{\vec{k}, \mu, \nu} a_{\mu}^{l_1}(\vec{k}) a_{\mu}^{l_2*}(\vec{k}) a_{\nu}^{l_3}(\vec{k} + \vec{q}) a_{\nu}^{l_4*}(\vec{k} + \vec{q}) \\
&\quad \times \frac{f(E_{\nu}(\vec{k} + \vec{q})) - f(E_{\mu}(\vec{k}))}{E_{\nu}(\vec{k} + \vec{q}) - E_{\mu}(\vec{k})} \quad (5)
\end{aligned}$$

where matrix elements $a_{\mu}^l(\vec{k})$ resulting from the diagonalization of the initial Hamiltonian H_0 connect orbital and band-space denoted by indices l and μ respectively. The E_{μ} are the eigenvalues of H_0 and $f(E)$ is the Fermi function. N is the number of sites in the unit cell. Temperature enters the calculation through the Fermi functions.

In the next step, the static spin- and orbital-susceptibilities ($\chi^{s, \text{RPA}}$ and $\chi^{c, \text{RPA}}$) are constructed in an RPA framework. The structure of the interaction matrices U^s and U^c can be inferred from Eq. 4 (see Ref. 100).

$$\left[\chi_{l_1 l_2 l_3 l_4}^{s, \text{RPA}}(\vec{q}) \right]^{-1} = \left[\chi_{l_1 l_2 l_3 l_4}^0(\vec{q}) \right]^{-1} - U_{l_1 l_2 l_3 l_4}^s \quad (6a)$$

$$\left[\chi_{l_1 l_2 l_3 l_4}^{c, \text{RPA}}(\vec{q}) \right]^{-1} = \left[\chi_{l_1 l_2 l_3 l_4}^0(\vec{q}) \right]^{-1} + U_{l_1 l_2 l_3 l_4}^c \quad (6b)$$

The pairing vertex in orbital space for the spin-singlet channel can be calculated using the fluctuation exchange approximation, which uses the previously calculated RPA susceptibilities. In the pairing vertex momenta \vec{k} and \vec{k}' are restricted to the Fermi surface.

$$\begin{aligned}
\Gamma_{l_1 l_2 l_3 l_4}(\vec{k}, \vec{k}') &= \left[\frac{3}{2} U^s \chi^{s, \text{RPA}}(\vec{k} - \vec{k}') U^s + \frac{1}{2} U^s \right. \\
&\quad \left. - \frac{1}{2} U^c \chi^{c, \text{RPA}}(\vec{k} - \vec{k}') U^c + \frac{1}{2} U^c \right]_{l_1 l_2 l_3 l_4} \quad (7)
\end{aligned}$$

The pairing vertex in orbital space is transformed into band space using the matrix elements $a_{\mu}^l(\vec{k})$.

$$\begin{aligned}
\Gamma_{\mu\nu}(\vec{k}, \vec{k}') &= \text{Re} \sum_{l_1 l_2 l_3 l_4} a_{\mu}^{l_1, *}(\vec{k}) a_{\mu}^{l_2, *}(-\vec{k}) [\Gamma_{l_1 l_2 l_3 l_4}(\vec{k}, \vec{k}')] \\
&\quad \times a_{\nu}^{l_3}(\vec{k}') a_{\nu}^{l_4}(-\vec{k}') \quad (8)
\end{aligned}$$

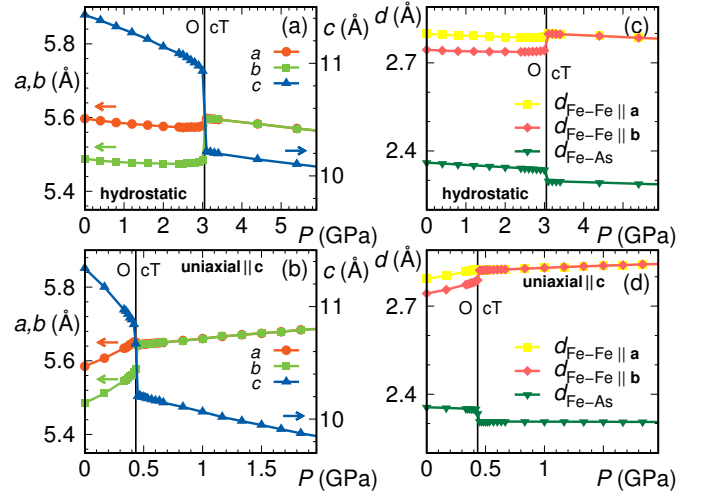


FIG. 2: Structure parameters of CaFe_2As_2 under application of hydrostatic (top row) and uniaxial pressure (bottom row). Shown are *ab-initio* calculated lattice parameters (a, b), and Fe-Fe and Fe-As bond lengths (c, d) within DFT (GGA). Reprinted with permission from Ref. 103.

Finally, one solves the linearized gap equation

$$-\sum_{\nu} \oint_{C_{\nu}} \frac{dk'_{\parallel}}{2\pi} \frac{1}{2\pi v_F(\vec{k}')} \left[\Gamma_{\mu\nu}(\vec{k}, \vec{k}') \right] g_i(\vec{k}') = \lambda_i g_i(\vec{k}) \quad (9)$$

by performing an eigendecomposition on the kernel and obtains the dimensionless pairing strength λ_i and the symmetry function $g_i(\vec{k})$. The integration runs over the discretized Fermi surface and $v_F(\vec{k})$ is the magnitude of the Fermi velocity.

This method of calculating the superconducting order parameter and pairing strength is appropriate when the pairing interaction quickly drops as a function of frequency, i.e. only Fermi surface pairing plays a role. In situations where bands away from the Fermi level are expected to contribute to the pairing, a frequency-dependent formulation has to be employed.

3. SIMULATING THE EFFECTS OF PRESSURE

We review here CaFe_2As_2 and BaFe_2As_2 as representative examples of the 122 family regarding pressure effects and the corresponding theoretical simulations with special emphasis on the origin and consequences of the appearance of a collapsed tetragonal phase.

Under hydrostatic pressure the c -axis of CaFe_2As_2 undergoes a contraction at a more rapid rate than the ab -plane [see Fig. 2(a)]¹⁰³. This is to be expected as 122 compounds don't have any chemical bonds oriented along the c -axis, and thus all structural deformations along the c -axis are bond-bending and low in energy. This is not the case for the ab -plane, where Fe-Fe bonds orient along the a and b -axes. At around 3.1 GPa the distance be-

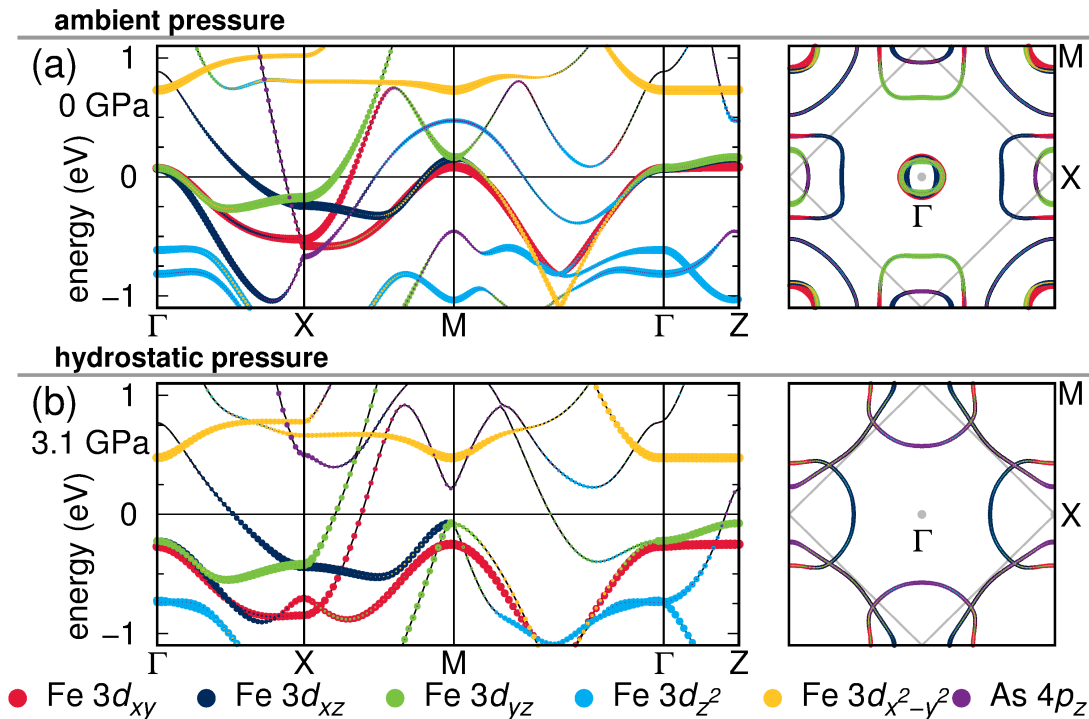


FIG. 3: Electronic structure of CaFe_2As_2 under hydrostatic pressure calculated from DFT (GGA). The band structure and the Fermi surface are shown in the large Brillouin zone corresponding to the 1Fe unit cell. Reprinted with permission from Ref. 103.

tween the two adjacent tri-layers becomes small enough that interlayer As p -As p bonds form and the c -axis undergoes a sharp collapse of 6.5%. At the same time the b -axis abruptly expands to assume the same length as the a -axis. In total the unit cell volume drops by 4.3% [see Fig. 2(c)] and the symmetry becomes tetragonal in absence of magnetism. The ratio $c/a_t = 2.58$ [see Fig. 2(c)], with $a_t = a/\sqrt{2}$, of the tetragonal cell indicates the structural collapse. This is in good qualitative agreement with experimental observations¹². The overestimation of the transition pressure, which is experimentally determined to be around 0.5 GPa, is also observed in other theoretical studies^{104,105}, and is the consequence of the sharp first order nature of the transition. The estimated bulk modulus at ambient pressure is 70 ± 3 GPa, in good agreement with the experimentally observed value¹⁰⁶, and it increases to 105 ± 2 GPa at the transition to the collapsed tetragonal phase.

The Fe-As bond lengths undergo a contraction in the entire pressure range, with a sharp drop at the transition pressure. In terms of a local moment picture, this leads to an increased crystal field splitting, and a subsequent suppression of the iron magnetic moments, which is consistent with the observed lack of magnetic order in the collapsed tetragonal phase.

In terms of the electronic structure, the increase of pressure pushes the t_{2g} band manifold towards lower energies as seen in Fig. 3(a), resulting in reduced contri-

butions of d_{xy} , d_{xz} and d_{yz} orbitals to the Fermi level density of states. At the same time, this means that the hole Fermi surface pockets around the Γ point become smaller, while the electron pockets around the \bar{X} point become larger [see Fig. 3(b)]. The label \bar{X} denotes the X -point of the Brillouin zone commensurate with the unit cell of the iron sublattice (the so-called 1Fe unit cell). An immediate consequence is the worsening of Fermi surface nesting, which leads to a weakening of the spin density wave state. Going deeper into the collapsed tetragonal phase, the three dimensionality of the Fermi surface becomes more pronounced as the tri-layers come closer.

Because of the inability to perform the ARPES experiments under pressure, a direct experimental observation of the aforementioned Fermi surface effects is not straightforward. However, due to the sharp first order nature of the phase transition in CaFe_2As_2 , it was shown that stabilization of the collapsed tetragonal phase is possible through postgrowth annealing and quenching of the samples¹⁰⁷⁻¹⁰⁹. Through the rapid quenching from high temperature, CaFe_2As_2 samples were essentially frozen in the metastable internally strained state, such that they do not revert to the orthorhombic phase upon cooling. Band dispersions observed with ARPES were shown to be in excellent agreement with the theoretically predicted picture¹¹⁰.

⁵⁷Fe Mössbauer spectroscopy of the samples, in conjunction with ab-initio calculations, provides additional

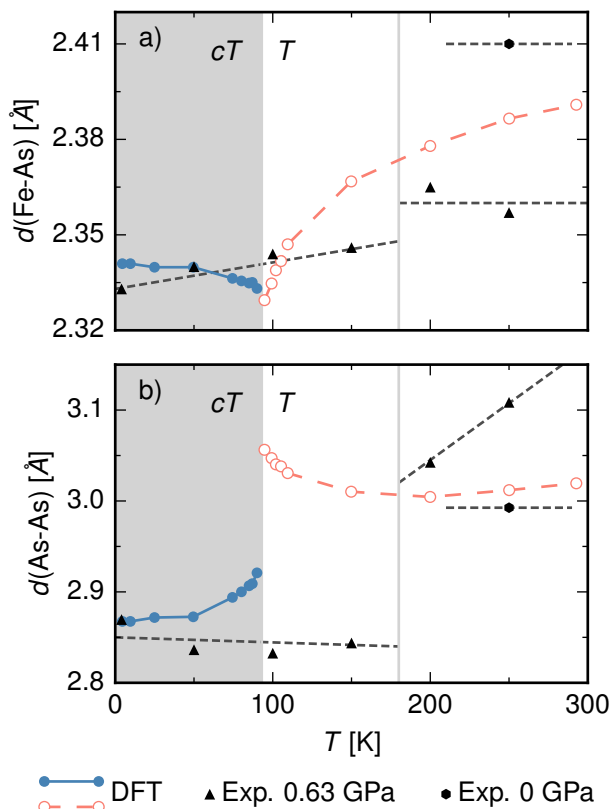


FIG. 4: Reconstruction of bond lengths in internally strained samples of CaFe_2As_2 from the ^{57}Fe Mössbauer spectroscopy. Shown are Fe-As bond lengths (a) and interlayer As-As bond lengths (b). The theoretical values were obtained within DFT (GGA). Reprinted with permission from Ref. 111.

insight into the microscopics of the collapsed tetragonal phase¹¹¹. Since Mössbauer spectroscopy probes properties intimately coupled to the electron charge density and the electric field gradients at the absorption nucleus¹¹² it provides valuable information about the immediate electronic environment of the iron nuclei. The Fe-As and interlayer As-As bond lengths deduced from Mössbauer spectroscopy (see Fig. 4) show a picture consistent with the behavior seen under pressure and provide insight into the physics behind the stabilization of the collapsed tetragonal phase. Namely, internally strained samples show relatively large interlayer As-As bond lengths, which further expand upon cooling. This results in charge saturation of the Fe-As bonds, which contract as the temperature is lowered. This process continues up to a point where it becomes energetically more favorable to transfer some of the charge from the Fe-As into the emptier interlayer As-As bond region, which prompts the formation of the interlayer As-As bonds and the formation of the collapsed tetragonal phase.

In BaFe_2As_2 the rates of contraction of both the c -axis and the ab -plane are faster with pressure than in CaFe_2As_2 [see Fig. 5(a)] as a consequence of a larger unit cell volume of BaFe_2As_2 due to the much larger size

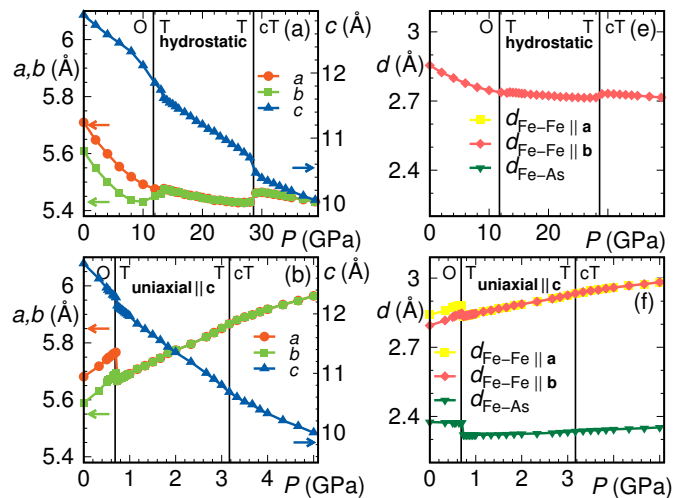


FIG. 5: Structure parameters of BaFe_2As_2 under application of hydrostatic (top row) and uniaxial pressure (bottom row). Shown are lattice parameters (a, b), and Fe-Fe and Fe-As bond lengths (c, d) calculated from DFT (GGA). Reprinted with permission from Ref. 103.

of the barium atom¹⁰³. Another consequence is that the formation of the collapsed tetragonal phase is delayed to much higher pressure of 28.6 GPa and is preempted by formation of an intermediate non-magnetic tetragonal phase at 11.75 GPa, which is consistent with other theoretical^{104,105} and experimental^{22,23} findings.

In contrast to the sharp first order transition seen in CaFe_2As_2 , the transition in BaFe_2As_2 is much more gradual and almost second order. The examination of the electronic structure shows that, in the case of BaFe_2As_2 , hole Fermi surface pockets around the Γ point get smaller and finally disappear, so that the Fermi surface is not nested any more. In consequence the spin density wave state is weakened beyond the point where magnetic order becomes unsustainable. Once the magnetic order disappears, BaFe_2As_2 becomes tetragonal again.

However, the interlayer As p -As p bonds still do not form and the theoretical results suggest a scenario where some residual local magnetic moments remain, sustaining the magnetic fluctuations. The role of temperature in the magnetic fluctuations has been examined in more detail by finite temperature and pressure molecular dynamics¹¹³. In such finite temperature calculations both the crystal structure and the magnetic moments are allowed to fluctuate. The magnitude of magnetic moments at $T = 5$ K is shown in Fig. 6. Around 12.5 GPa there is a transition to the low spin state, which persists up to about 20 GPa, where it is totally suppressed. This supports the fluctuating moment picture at finite temperature in the intermediate tetragonal phase. At $T = 0$ and a pressure of 28.6 GPa the distance between the tri-layers is reduced enough so that the interlayer As-As bonds can form around the barium atom.

The estimated ambient pressure bulk modulus is $67 \pm$

4 GPa, which increases to 128 ± 3 GPa for the intermediate tetragonal phase and up to 173 ± 2 GPa for the collapsed tetragonal phase, in excellent agreement with the measured values²².

We already mentioned the anisotropy of the 122 crystal structure and in particular the softness of the c -axis. Therefore, we investigated uniaxial pressure effects along the c -axis¹⁰³. The behavior of the unit cell of CaFe_2As_2 is shown in Fig. 2(b). There is a strong suppression of the c -axis and homogeneous expansion in the ab -plane until 0.48 GPa, where the c -axis collapses and the system enters the non-magnetic collapsed tetragonal phase. The order of magnitude reduction of transition pressure is in excellent agreement with the experimental observations¹⁵.

The electronic structure shows a complete suppression of the hole pockets around the Γ point while CaFe_2As_2 is still in the orthorhombic magnetic phase. However, if we compare the Fe-As bond lengths [see Figs. 2(a) and (b)], we see that under the c -axis uniaxial pressure the Fe-As bond suppression is slower, allowing for larger local moments due to the reduced crystal field splitting. Thus, although the Fermi surface is not nested, there is a large contribution of local moments maintaining the magnetic order.

For BaFe_2As_2 , the c -axis uniaxial pressure also results in an order of magnitude reduction of the transition pressure, both for the intermediate tetragonal and collapsed tetragonal phase, from 11.6 GPa to 0.72 GPa and from 28.6 GPa to 3.17 GPa, indicating that the larger size of BaFe_2As_2 does not have a detrimental effect for the anisotropy along the c -axis. The Fe-As bond lengths are not suppressed below 2.3 Å with c -axis uniaxial pressure, implying that the magnetic moments are more delocalized due to the more flat Fe-As tetrahedra. Increased sensitivity to the c -axis uniaxial pressure is consistent with the experimentally observed behavior²¹.

Application of compressive strain along the a -axis obviously results in suppression of the orthorhombicity and magnetic moment both in CaFe_2As_2 and BaFe_2As_2 , but only up to a certain pressure, at which it becomes energetically more favorable to rotate the magnetic order by 90 degrees⁸⁹. At this point, the a and b -axes switch their places and the orthorhombicity switches sign. This axis inversion is particularly interesting in the case of CaFe_2As_2 , where the magnetic moments have been shown to be quite fragile. It is also interesting to note that axis inversion in CaFe_2As_2 requires a larger pressure (0.67 GPa) than in BaFe_2As_2 (0.22 GPa). This is related to the fact that c -axis uniaxial pressure is much more effective at magnetic moment suppression for CaFe_2As_2 than the uniaxial pressure applied in the ab -plane. This is the opposite of what is observed in BaFe_2As_2 . Similarly, tensile strain applied along the shorter b -axis also results in axis inversion, with BaFe_2As_2 requiring lower pressure (-0.22 GPa) compared to CaFe_2As_2 (-0.33 GPa). This corresponds to the detwinning scenario where the orthorhombicity

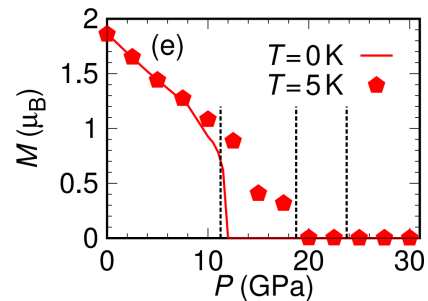


FIG. 6: Finite temperature magnetic moment of BaFe_2As_2 calculated from *ab-initio* molecular dynamics (DFT-GGA). Reprinted with permission from Ref. 113.

of one of the twin domains switches sign while the domain walls stay pinned. Our calculations showed a detwinning strain around 0.2 GPa, which is an order of magnitude larger than the detwinning strain needed in the tetragonal phase and is consistent with experimental observations^{30,114}. Phenomenological Ginzburg-Landau modelling of the magneto-elastic physics leading to the axis inversion suggested that the larger reversal pressure in CaFe_2As_2 implies a larger magneto-elastic coupling in CaFe_2As_2 than in BaFe_2As_2 ⁸⁹. This has a number of consequences^{33,115,116}, one of which is that the magneto-structural transitions in CaFe_2As_2 are first-order, while in BaFe_2As_2 they are more second-order like. Application of tensile strain in the ab -plane⁸⁹ results in suppression of hole pockets around the Γ point and in more pronounced overall three-dimensionality of the Fermi surface. Indeed c -axis uniaxial pressure also suppresses the Γ point hole pockets due to the involved in-plane expansion [see Figs. 2(b) and 5(b)].

4. EFFECTS OF ELECTRONIC CORRELATIONS

In this section we focus our attention on the role of correlations in representative systems of the 111, 1111 and 122 families.

LiFeAs. - We will first review the influence of electronic correlations in the iron-based superconductor LiFeAs and their effects on band structure and Fermi surface. Following our calculations based of LDA+DMFT⁵¹ in Fig. 7 we compare the spectral function for LiFeAs as obtained from LDA+DMFT with its LDA counterpart at a temperature of $T = 72.5$ K. The spectral function shows well defined excitations at the Fermi level, with increasing broadening due to the electronic correlations at higher binding energies, supporting the picture of well-defined quasiparticles at this temperature in this system. Therefore, this system shows characteristics of a Fermi-liquid state in a metal with moderate correlations without significant spectral weight transfer from the Fermi level to lower or higher binding energies.

In Fig. 8 we show the Fermi surface as obtained from

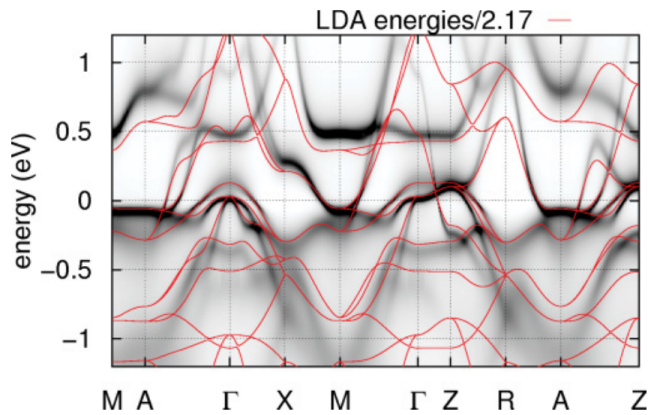


FIG. 7: Momentum resolved LDA+DMFT spectral function of LiFeAs compared to the LDA dispersion (red lines). The LDA bands have been renormalized by the orbitally averaged mass renormalization obtained from LDA+DMFT. Reprinted with permission from Ref. 51.

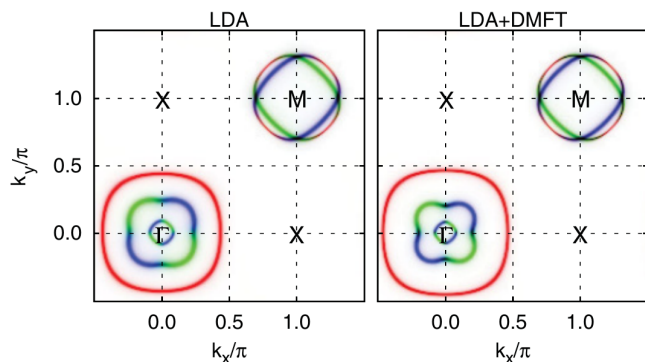


FIG. 8: LDA and LDA+DMFT Fermi surfaces at $k_z = 0$ for LiFeAs. The color code labels the orbital character: d_{xy} (red), d_{xz} (green) and d_{xz} (blue). Reprinted with permission from Ref. 51.

LDA+DMFT, which shows hole pockets around the Γ -point and electron pockets around the M -point. The electronic correlations cause the shrinking of the middle d_{xz}/yz hole pocket and an increase of the outer d_{xy} pocket, whereas the shape of the electron pockets is hardly affected. This result indicates that the electronic correlations tend to weaken Fermi surface nesting in this material or even might suppress it.

For a more quantitative comparison we calculated the dHvA frequencies from LDA+DMFT. The dHvA frequencies correspond to the extremal size of the Fermi surface pockets at a given angle with respect to the k_z axis. In Fig. 9 we compare our theoretical results to the experimental measurements from Ref. 42. Despite a few small differences, LDA seems to agree with experiment quite well.

Inclusion of electronic correlations induces a shrinking of the middle hole pocket as a downward shift of the corresponding frequency response, and an upward shift of the enlarged outer pocket. Ref. 42 assigns the measured

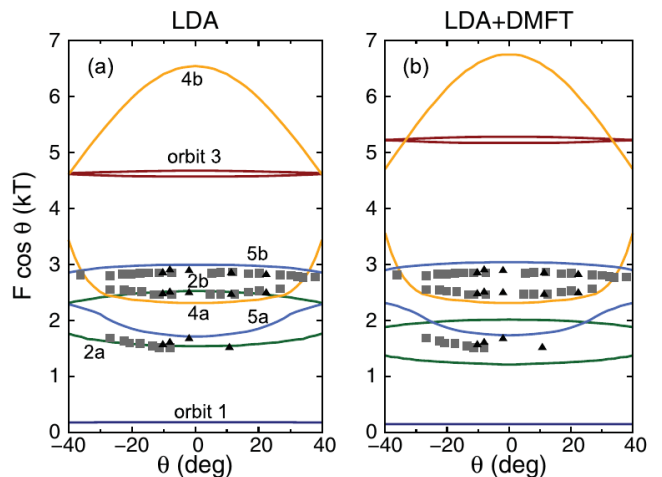


FIG. 9: dHvA frequencies for LiFeAs as a function of magnetic field angle. The solid lines refer to the theoretical calculation, while the points refer to the experimental data from Ref. 42. The theoretical data was obtained by calculating the angle-dependent extremal cross-sections of the Fermi surface cylinders from the DFT (left) or LDA+DMFT (right) calculation. Reprinted with permission from Ref. 51.

frequencies to the electron Fermi surface sheets, where the two higher frequencies are assigned to orbits 5b and 4a, and the lowest frequency is assumed to originate from orbit 5a¹¹⁷.

Our results support this interpretation: while the orbits 2a/5a and 2b/4a are of similar size in the LDA calculation, the hole pockets are modified and the near degeneracy in the de Haas-van Alphen frequency plot is lifted. Therefore, the electron orbits 2a and 2b are unlikely to give rise to the measured frequencies, as their sizes are rather different from the measured data. This finding reconciles theory and experiment. The shrunk middle hole pocket is only seen in ARPES, which finds a correlated metal with poor nesting together with sizable mass renormalization. In contrast, the dHvA measurement resolves the (lighter) electron pocket sizes in LiFeAs that almost do not change under inclusion of correlation. Recent LDA+DMFT calculations for LiFeAs^{47,118} show the same trends as our results⁵¹.

LiFeP and LaFePO. - As a comparison study, we review the LDA+DMFT calculations for LaFePO and LiFeP⁵². Fig. 10 shows the momentum resolved spectral function for both materials and the comparison to the LDA result. Both compounds show a distinctive change in the topology of the Fermi surface with a hole pocket of Fe d_{z^2} orbital character changing from a closed shape in LDA to an open shape in LDA+DMFT. This change of topology occurs around the Γ (Z) point in LaFePO (LiFeP).

This effect is clearly visible in the calculated Fermi surface. Fig. 11 shows the appearance of an additional outer hole pocket at Γ in LaFePO and an inner hole pocket at Z in LiFeP⁵². As discussed by Kemper *et al.*¹¹⁹, this might promote a nodal gap and weaken the pairing strength, in

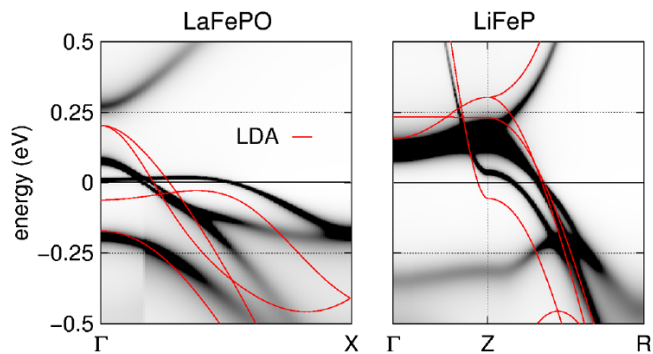


FIG. 10: Momentum resolved LDA+DMFT spectral function of LaFePO (left) and LiFeP (right) together with the LDA bands close to the Fermi surface topology change. Reprinted with permission from Ref. 52.

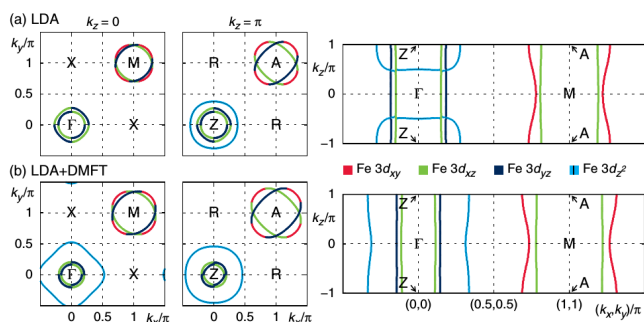


FIG. 11: Fermi surfaces for LaFePO in the $k_z = 0, \pi$ plane (left) and $k_x = k_y$ plane (right). The upper row shows the result obtained from DFT, while the lower row shows the modified Fermi surface including electronic correlations on the LDA+DMFT level. The colors indicate the orbital character. Reprinted with permission from Ref. 52.

turn also lowering the superconducting transition temperature. In conclusion, while LiFeP and LaFePO are less correlated than LiFeAs (band renormalizations and effective masses are smaller), correlation effects are crucial to understand the topology of the Fermi surface.

CaFe₂As₂.- We proceed now with the 122 family and the interplay between correlation effects and pressure. We consider here *CaFe₂As₂* as a representative system, where we review the effects of correlation between the tetragonal and the collapsed tetragonal phase as discussed in Refs. 121,122. In contrast to the previous materials, the topology of the Fermi surface in both phases remains nearly unaffected upon the inclusion of electronic correlations. This manifests in the orbital-selective mass renormalizations of a factor of 1.3 to 1.7 introduced by LDA+DMFT.

Nonetheless, these results improve the agreement of the calculations with ARPES experiments¹¹⁰ compared to the pure LDA result, since the bandwidth renormalization obtained in experiment is quite well reproduced by the calculation. In Fig. 12 we show the results for the momentum-resolved spectral function in both the

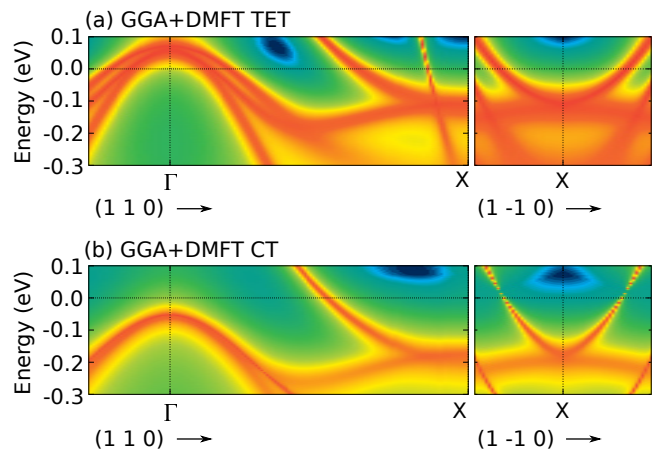


FIG. 12: Momentum resolved LDA+DMFT spectral function for *CaFe₂As₂* in the tetragonal and collapsed tetragonal phase. Reprinted with permission from Ref. 120.

tetragonal and collapsed tetragonal phase. The tetragonal phase shows three hole pockets at the Γ -point and two electron pockets at the M -point, whereas in the collapsed tetragonal phase the hole pockets are pushed below the Fermi level and thus vanish, while the electron pockets increase significantly in size.

The influence of the tetragonal to collapsed tetragonal transition on the orbital-dependent effective masses manifests in a decrease of electronic correlation effects, where the Fe $3d_{xy}$ orbital changes from being the most strongly correlated orbital in the tetragonal phase to being the least correlated one in the collapsed tetragonal phase. This change is due to the increase in hybridization of the Fe $3d$ orbitals after the structural collapse. The decreased distance of the Fe-As layers enforces hybridization of the Fe $3d_{xy}$ -Fe $3d_{xy}$ as well as Fe $3d_{xy}$ -As $4p_x$ and $4p_y$ orbitals. This reduces the localization of the electrons and renders the Fe $3d_{xy}$ less localized (and thus less correlated). In conclusion, electronic correlation effects are important even for weakly correlated pnictides like *CaFe₂As₂* in order to understand the orbital-selective mass renormalizations that are seen in ARPES measurements.

KFe₂As₂.- We now move to the description of our results obtained for the hole-doped iron-pnictide superconductor *KFe₂As₂*⁹³. Especially for this material, DFT calculations are insufficient to satisfactorily describe angle-resolved photoemission (ARPES) measurements as well as observed de Haas van Alphen (dHvA) frequencies.

In our LDA+DMFT calculations reported in Ref. 93 we find that *KFe₂As₂* is a moderately to strongly correlated metal with a mass renormalization factor of the Fe $3d$ orbitals between 1.6 and 2.7. The observed strong flattening of electronic bands due to the renormalization is a possible explanation for the spread of experimental results in this compound in terms of extreme sensitivity to the experimental stoichiometry. We find significant

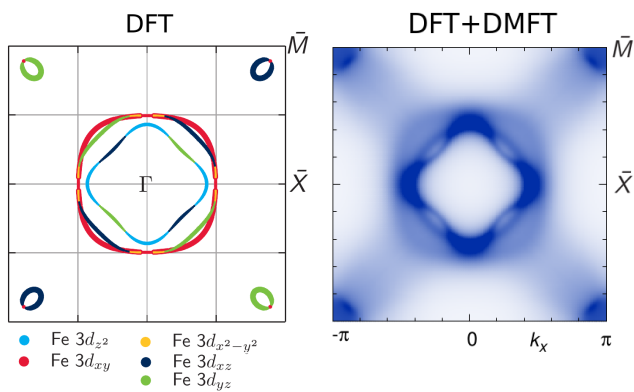


FIG. 13: Fermi surface at $k_z = 0$ of KFe_2As_2 as obtained from DFT (left) and the momentum resolved spectral function at the Fermi level as obtained from LDA+DMFT (right). Reprinted with permission from Ref. 93.

modifications in the size and shape of the Fermi surface pockets, which in this system are only composed of hole pockets.

In Fig. 13 we show a comparison between the Fermi surface obtained from DFT and LDA+DMFT at $k_z = 0$. The DFT result contains a middle hole cylinder at Γ , which is too large compared to ARPES^{37,38}. Correlations within LDA+DMFT increase the size of the outer cylinder while reducing the size of the middle, and also modifies the shape of the inner cylinder, which greatly improves the agreement with the ARPES measurements. Additionally, we predict a topological change with respect to DFT calculations, namely the opening of an inner hole cylinder at the Z point. As a result, we also found that our calculated dHvA frequencies are modified by electronic correlations and qualitatively agree with experimental data^{40,43}. Furthermore, the intersection nodes on the inner two hole cylinders offer a natural explanation for magnetic breakdown orbits observed in the dHvA measurements⁴³.

On this basis, we argue that correlation effects are important and a necessary ingredient in understanding the electronic structure in KFe_2As_2 , as well as the presently under debate nature of the superconducting state in KFe_2As_2 .

AFe₂As₂ (A = K, Rb, Cs). - In our previous studies, for example in CaFe_2As_2 ¹²⁰ and KFe_2As_2 ⁹³, which showed that: (i) a compression of the unit cell in general reduces the strength of electronic correlations and (ii) the hole doping of the parent compound BaFe_2As_2 by substituting Ba by K yields a moderately to strongly correlated system with notable correlation effects in the electronic structure.

This naturally raises the question whether a decompression, i.e. increase of the interatomic distances in the unit cell increases the electronic correlations as opposed to a reduction found under a compression of the unit cell. Guided by this question we investigate via LDA+DMFT the manifestation of correlation effects in

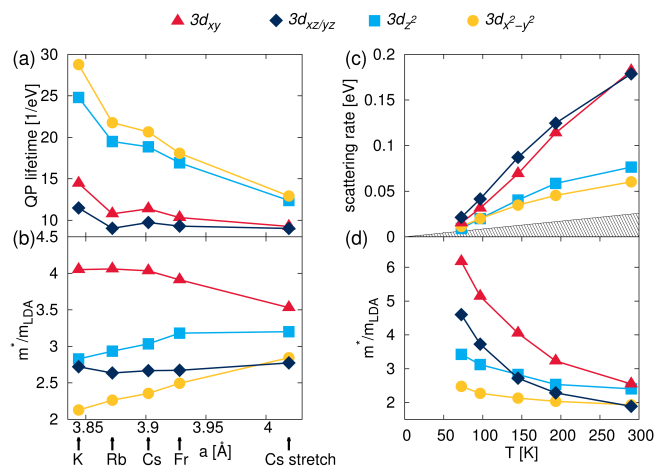


FIG. 14: The quasiparticle lifetime (a) and mass enhancements (b) as obtained from LDA+DMFT as a function of increasing atomic radius in the $A\text{Fe}_2\text{As}_2$ ($A=\text{K}, \text{Rb}, \text{Cs}, \text{Fr}$). The temperature dependence of the scattering rate (c) and mass enhancement (d) for the example of KFe_2As_2 shows that these systems are quite deep in the incoherent regime with a coherence temperature of about 50 K. Reprinted with permission from Ref. 123.

a wide range of binding energies in the hole-doped family of Fe-pnictides $A\text{Fe}_2\text{As}_2$ ($A = \text{K}, \text{Rb}, \text{Cs}$) as well as the fictitious FrFe_2As_2 and a -axis stretched CsFe_2As_2 . This choice of systems allows for a systematic analysis of the interplay of Hund's coupling J_H and on-site Coulomb repulsion U in multi-orbital Fe-pnictides under *negative* pressure, described in detail in Ref. 123.

When increasing the ionic size of the alkali metal, we observe (i) a non-trivial change in the iron $3d$ hoppings, (ii) an increase of orbitally-selective correlations and (iii) transfer of incoherent spectral weight to high-binding energies. We do not find the typical lower Hubbard-band, but rather characteristic features of a Hund's metal. This is especially prominent in a -stretched CsFe_2As_2 . We also find that the coherent/incoherent electronic behavior of the systems depends, apart from temperature, also strongly on J_H . To elucidate this, we show the quasiparticle lifetime and the orbitally resolved effective masses as a function of atomic radius in Fig. 14(a) and (b).

We find a strong suppression of the quasiparticle lifetimes for larger atomic radius, as well as an overall increase in electronic correlations. From our analysis of the electronic properties in a wide range of binding energies, we come to the conclusion that along the isoelectronic doping series $A\text{Fe}_2\text{As}_2$ ($A = \text{K}, \text{Rb}, \text{Cs}$), and also for the fictitious FrFe_2As_2 and a -axis stretched CsFe_2As_2 , correlation and incoherence of the Fe $3d$ orbitals increase, albeit orbitally selective.

These systems show distinctive features of Hund's metals, i.e. the Hund's coupling J_H plays a major role in the strength of correlations and especially coherence. Therefore, these materials are much more incoherent than expected from the value of the Coulomb repulsion U alone.

While the most correlated orbitals (d_{xy}) show features that resemble those of being close to an orbital selective Mott transition, especially for a -stretched CsFe_2As_2 , the system is quite deep in the incoherent bad metal regime with a finite spectral weight at the Fermi level even when we vary the interaction parameters in the range from $U = 4$ eV, $J_H = 0.8$ eV and $U = 6$ eV, $J_H = 1.2$ eV. This actually shows that the systems are not close to an orbital selective Mott transition, but rather are highly incoherent due to the suppression of orbital fluctuations by the Hund's coupling at the temperature considered.

We predict that by increasing the Fe-Fe distance experimentally in the most correlated and incoherent system CsFe_2As_2 , e.g. by stretching, will induce an orbital dependent increase in correlations and incoherence of the Fe 3d orbitals, where the Fe $3d_{z^2}$ and Fe $3d_{xy}$ orbitals are strongly but not fully localized and the other Fe 3d orbitals retain a bad metallic behavior. From our results of the temperature dependence of the scattering rate shown in Fig. 14(c) we estimate the coherence temperature to be located around 50 K in KFe_2As_2 and even lower for RbFe_2As_2 and CsFe_2As_2 . This agrees qualitatively with experimental observations^{44,45}.

The incoherent properties also render the usual way of obtaining the mass enhancements by the slope of the self-energy invalid, which assumes Fermi liquid properties. These are clearly violated if the imaginary part of the self-energy takes on a finite value for $\omega \rightarrow 0$, i.e. has a significant scattering rate.

Therefore, we conclude that especially the hole doped end systems of the 122 iron pnictide family KFe_2As_2 , RbFe_2As_2 and CsFe_2As_2 , as well as the a -axis stretched CsFe_2As_2 are a valuable test bed to study the features of strongly correlated Hund's metals and orbital-selective bad metallicity and its interplay with superconductivity.

5. SUPERCONDUCTIVITY

In this section we concentrate on our work on superconductivity in extremely hole- and electron-doped iron pnictides and chalcogenides. Our investigations were driven by experimental progress in application of pressure and sample preparation. In the following subsections we review the experimental situation in extremely hole-doped iron pnictides under high pressures and the current status of iron selenide and intercalates. We put our work into the context provided by the relevant experiments.

Extremely hole-doped iron pnictides under pressure.— The phase diagram, and in particular the normal state properties, of the $A\text{Fe}_2\text{As}_2$ ($A = \text{Ca}, \text{Ba}, \text{K}, \text{Rb}, \text{Cs}, \text{Fr}$) family of materials have been discussed extensively in the previous sections. In this subsection we concentrate on the KFe_2As_2 material, which superconducts below a critical temperature $T_c = 3.4$ K⁶⁴. For moderate pressures a V-shaped dependence of T_c has been observed in some experiments^{64,124,125}, while no such behavior is found un-

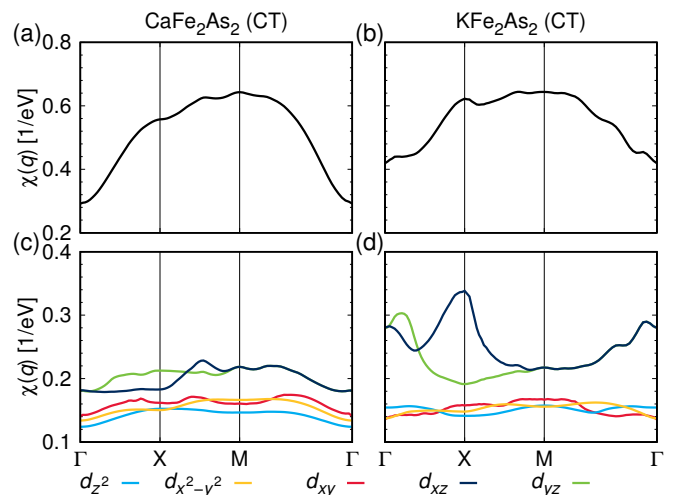


FIG. 15: Summed static susceptibility (top) and its diagonal components χ_{aa}^{aa} (bottom) in the eight-band tight-binding model for [(a) and (c)] CaFe_2As_2 and [(b) and (d)] KFe_2As_2 in the one-Fe Brillouin zone, based on DFT (GGA). The colors identify the Fe 3d states. Reprinted with permission from Ref. 128.

der slightly different experimental conditions^{126,127}. Surprisingly, at high pressures a superconducting phase with T_c of up to 12 K was found^{126,127}, which is linked to a structural collapse as it is known from CaFe_2As_2 and BaFe_2As_2 .

From our previous work we know that correlation effects are extremely important in KFe_2As_2 and that even the Fermi surface from pure DFT is incorrect⁹³. At large pressures one can however expect the electronic bandwidth to increase and correlation effects to diminish in consequence. We find that this is indeed the case for the high pressure collapsed phase of KFe_2As_2 based on lattice parameters taken from Ref. 126. In fact, the Fermi surface of the collapsed phase is insensitive to inclusion of correlation effects¹²⁸.

Performing DFT calculations in the GGA approximation we furthermore find that a Lifshitz transition is associated with the structural collapse¹²⁸. The electronic structure on the low-pressure side of the phase transition is qualitatively the same as that at zero pressure, while in the collapsed phase it is similar to that of CaFe_2As_2 , but with additional small hole pockets in the Brillouin zone center. We showed that this difference is crucial for establishing nesting with wave vector $X = (\pi, 0)$, as evidenced in the static spin-susceptibility (see Fig. 15). From RPA we have predicted unconventional superconductivity with a sign-changing s_{\pm} order parameter to be realized in the collapsed phase of KFe_2As_2 ¹²⁸, while the non-collapsed phase is a d -wave superconductor (see also Refs. 129,130 for ambient pressure results). Therefore, the structural collapse does not only induce a Lifshitz transition, but also changes the symmetry of the superconducting state from d -wave to extended s -wave (see

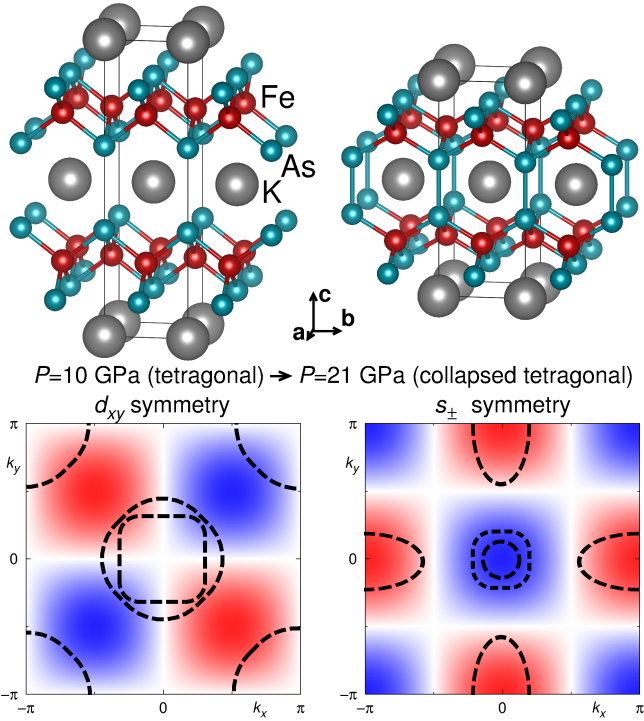


FIG. 16: Crystal structure, schematic Fermi surface (dashed lines) and schematic superconducting gap function (background color) of KFe_2As_2 in the one-Fe Brillouin zone before and after the volume collapse. The Lifshitz transition associated with the formation of As $4p_z$ -As $4p_z$ bonds in the CT phase changes the superconducting pairing symmetry from d_{xy} to s_{\pm} . Reprinted with permission from Ref. 128.

Fig. 16).

The observation that small hole pockets at the Brillouin zone center re-emerge under pressure could also explain why superconductivity has been found in the collapsed phase of CaFe_2As_2 under uniaxial pressure, but not under hydrostatic conditions. We have shown previously that uniaxial pressure quickly leads to the re-emergence of hole pockets at the Brillouin zone center in this compound¹⁰³.

Pressure and doping in iron selenide.- Iron-based superconductors are not only amenable to modification by application of pressure, but also by charge doping. The effects of both are evidenced prominently in the iron selenide material.

While unpressurized bulk FeSe has a T_c of 8-10 K, pressure enhances the critical temperature to about $T_c \sim 40$ K¹³¹. This comes entirely unexpected, as most other iron-based superconductors are thought to have an antiferromagnetic parent state, which can be suppressed by application of pressure. Pressing further, the superconducting critical temperature also decreases in these compounds. In FeSe instead of an antiferromagnetic dome, a large C_2 -symmetric nematic region is found, where the crystal structure is already orthorhombic, but no static magnetism is realized.

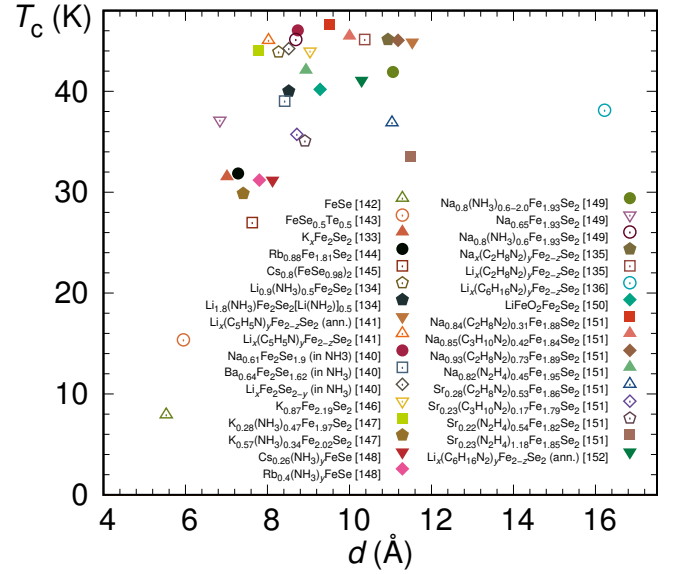


FIG. 17: Relationship between the maximum T_c and the interlayer spacing in intercalated FeSe-based superconductors.

We recently found that FeSe is subject to an unexpected magnetic frustration not found in other iron-based superconductors. In Ref. 132 we show that a $J_1 - J_2 - J_3$ exchange model with additional biquadratic term K accurately describes the non-monotonic pressure dependence of superconductivity and the orbital ordered nematic region in FeSe.

Another possibility to modify FeSe is electron doping. It was recently shown that various alkali atoms and organic molecules can be intercalated between the layers of bulk FeSe by different chemical processes^{133–141}. In this way, T_c can be enhanced to up to 46 K without application of pressure. Noji *et al.*^{135,136} correlated T_c with enhanced interlayer spacing due to intercalation (see Fig. 17 where data from Refs. 133–136,140–152 have been plotted), but could not explain the wide variation of transition temperatures found upon intercalation of different combinations of alkali atoms and organic solvents.

We performed DFT calculations for lithium and ammonia intercalated FeSe and showed that the initial rise of T_c up to an interlayer spacing of about 9 Å can be explained with an increasingly two-dimensional electronic structure¹⁵³. Beyond an interlayer distance of 9 Å the electronic structure is entirely two-dimensional and no further increase of T_c can be expected through this mechanism. Using RPA calculations we furthermore find that the electron doping significantly modifies the superconducting pairing strength, and hence T_c , through a density of states effect as the upper edge of the hole bands moves closer to the Fermi level. Naturally this effect is also limited by the disappearance of hole pockets upon further electron doping.

Our predictions have been subsequently confirmed by various experimental groups, who could not enhance the transition temperatures by separating the FeSe layers fur-

ther, but found a strong dependence of T_c on the number of electrons doped^{149,151,152,154}. A large number of FeSe intercalates has been synthesized meanwhile, but T_c empirically seems to be limited to ≤ 46 K.

6. CONCLUSIONS

We reviewed the properties of iron-based superconductors under application of pressure and chemical doping. We discussed the influence of pressure on structural details of the 122 family of iron pnictides and in particular the emergence of the volume collapsed phase. Based on DFT+DMFT calculations we elucidated the issue of bad metallicity and its connection to Hund's rule coupling in a broad range of iron-based materials, in particular the hole-doped end members of the 122 series. Furthermore,

we reviewed the nematic state and non-monotonous pressure dependence of superconductivity in bulk iron selenide. Finally we discussed the superconducting properties of a hole-doped 122 material and the intercalated iron selenides.

Acknowledgments

The work presented in this review was made possible by the financial support provided by the German Research Foundation (Deutsche Forschungsgemeinschaft) through priority program SPP 1458. The authors thank Bernd Büchner, Rudi Hackl, Carsten Honerkamp and Dirk Johrendt for initiating this priority program and for important discussions.

-
- ¹ Y. Kamihara, T. Watanabe, M. Hirano, and H. Hosono, *J. Am. Chem. Soc.* **130**, 3296 (2008).
- ² R. Hoffmann and C. Zheng, *J. Phys. Chem.* **89**, 4175 (1985).
- ³ I. Opahle, H. C. Kandpal, Y. Zhang, C. Gros, and R. Valentí, *Phys. Rev. B* **79**, 024509 (2009).
- ⁴ N. Ni, S. Nandi, A. Kreyssig, A. I. Goldman, E. D. Mun, S. L. Bud'ko, and P. C. Canfield, *Phys. Rev. B* **78**, 014523 (2008).
- ⁵ A. I. Goldman, D. N. Argyriou, B. Ouladdiaf, T. Chatterji, A. Kreyssig, S. Nandi, N. Ni, S. L. Bud'ko, P. C. Canfield, and R. J. McQueeney, *Phys. Rev. B* **78**, 100506 (2008).
- ⁶ G. Wu, H. Chen, T. Wu, Y. L. Xie, Y. J. Yan, R. H. Liu, X. F. Wang, J. J. Ying, and X. H. Chen, *J. Phys.: Condens. Matter* **20**, 422201 (2008).
- ⁷ F. Ronning, T. Klimczuk, E. D. Bauer, H. Volz, and J. D. Thompson, *J. Phys.: Condens. Matter* **20**, 322201 (2008).
- ⁸ P. C. Canfield, S. L. Bud'ko, N. Ni, A. Kreyssig, A. I. Goldman, R. J. McQueeney, M. S. Torikachvili, D. N. Argyriou, G. Luke, and W. Yu, *Physica C* **469**, 404 (2009).
- ⁹ M. Alzamora, J. Munevar, E. Baggio-Saitovitch, S. L. Bud'ko, N. Ni, P. C. Canfield, and D. R. Sanchez, *J. Phys.: Condens. Matter* **23**, 145701 (2011).
- ¹⁰ W. Yu, A. A. Aczel, T. J. Williams, S. L. Bud'ko, N. Ni, P. C. Canfield, and G. M. Luke, *Phys. Rev. B* **79**, 020511 (2009).
- ¹¹ H. Lee, E. Park, T. Park, V. A. Sidorov, F. Ronning, E. D. Bauer, and J. D. Thompson, *Phys. Rev. B* **80**, 024519 (2009).
- ¹² A. Kreyssig, M. A. Green, Y. Lee, G. D. Samolyuk, P. Zajdel, J. W. Lynn, S. L. Bud'ko, M. S. Torikachvili, N. Ni, S. Nandi, et al., *Phys. Rev. B* **78**, 184517 (2008).
- ¹³ M. S. Torikachvili, S. L. Bud'ko, N. Ni, and P. C. Canfield, *Phys. Rev. Lett.* **101**, 057006 (2008).
- ¹⁴ A. I. Goldman, A. Kreyssig, K. Proke, D. K. Pratt, D. N. Argyriou, J. W. Lynn, S. Nandi, S. A. J. Kimber, Y. Chen, Y. B. Lee, et al., *Phys. Rev. B* **79**, 024513 (2009).
- ¹⁵ K. Prokeš, A. Kreyssig, B. Ouladdiaf, D. K. Pratt, N. Ni, S. L. Bud'ko, P. C. Canfield, R. J. McQueeney, D. N. Argyriou, and A. I. Goldman, *Phys. Rev. B* **81**, 180506 (2010).
- ¹⁶ M. S. Torikachvili, S. L. Bud'ko, N. Ni, P. C. Canfield, and S. T. Hannahs, *Phys. Rev. B* **80**, 014521 (2009).
- ¹⁷ M. Rotter, M. Tegel, D. Johrendt, I. Schellenberg, W. Hermes, and R. Pttgen, *Phys. Rev. B* **78**, 020503 (2008).
- ¹⁸ E. Colombier, S. L. Bud'ko, N. Ni, and P. C. Canfield, *Phys. Rev. B* **79**, 224518 (2009).
- ¹⁹ P. L. Alireza, Y. T. C. Ko, J. Gillett, C. M. Petrone, J. M. Cole, G. G. Lonzarich, and S. E. Sebastian, *J. Phys.: Condens. Matter* **21**, 012208 (2009).
- ²⁰ J. Paglione and R. L. Greene, *Nat. Phys.* **6**, 645 (2010).
- ²¹ W. Uhoya, G. Tsoi, Y. K. Vohra, M. A. McGuire, A. S. Sefat, B. C. Sales, D. Mandrus, and S. T. Weir, *J. Phys.: Condens. Matter* **22**, 292202 (2010).
- ²² R. Mittal, S. K. Mishra, S. L. Chaplot, S. V. Ovsyannikov, E. Greenberg, D. M. Trots, L. Dubrovinsky, Y. Su, T. Brueckel, S. Matsuishi, et al., *Phys. Rev. B* **83**, 054503 (2011).
- ²³ S. A. J. Kimber, A. Kreyssig, Y.-Z. Zhang, H. O. Jeschke, R. Valentí, F. Yokaichiya, E. Colombier, J. Yan, T. C. Hansen, T. Chatterji, et al., *Nat. Mater.* **8**, 471 (2009).
- ²⁴ J.-H. Chu, J. G. Analytis, D. Press, K. de Greve, T. D. Ladd, Y. Yamamoto, and I. R. Fisher, *Phys. Rev. B* **81**, 214502 (2010).
- ²⁵ M. A. Tanatar, E. C. Blomberg, A. Kreyssig, M. G. Kim, N. Ni, A. Thaler, S. L. Bud'ko, P. C. Canfield, A. I. Goldman, I. I. Mazin, et al., *Phys. Rev. B* **81**, 184508 (2010).
- ²⁶ H.-H. Kuo, J.-H. Chu, S. C. Riggs, L. Yu, P. L. McMahon, K. de Greve, Y. Yamamoto, J. G. Analytis, and I. R. Fisher, *Phys. Rev. B* **84**, 054540 (2011).
- ²⁷ T. Liang, M. Nakajima, K. Kihou, Y. Tomioka, T. Ito, C. H. Lee, H. Kito, A. Iyo, H. Eisaki, T. Kakeshita, et al., *J. Phys. Chem. Solids* **72**, 418 (2011).
- ²⁸ C. Dhital, Z. Yamani, W. Tian, J. Zeretsky, A. S. Sefat, Z. Wang, R. J. Birgeneau, and S. D. Wilson, *Phys. Rev. Lett.* **108**, 087001 (2012).
- ²⁹ E. C. Blomberg, A. Kreyssig, M. A. Tanatar, R. M. Fernandes, M. G. Kim, A. Thaler, J. Schmalian, S. L. Bud'ko, P. C. Canfield, A. I. Goldman, et al., *Phys. Rev. B* **85**,

- 144509 (2012).
- ³⁰ J.-H. Chu, H.-H. Kuo, J. G. Analytis, and I. R. Fisher, *Science* **337**, 710 (2012).
- ³¹ C. Fang, H. Yao, W.-F. Tsai, J. Hu, and S. A. Kivelson, *Phys. Rev. B* **77**, 224509 (2008).
- ³² C. Xu, M. Mller, and S. Sachdev, *Phys. Rev. B* **78**, 020501 (2008).
- ³³ R. M. Fernandes, L. H. Vanbebber, S. Bhattacharya, P. Chandra, V. Keppens, D. Mandrus, M. A. McGuire, B. C. Sales, A. S. Sefat, and J. Schmalian, *Phys. Rev. Lett.* **105**, 157003 (2010).
- ³⁴ H. H. Kuo, J. G. Analytis, J. H. Chu, R. M. Fernandes, J. Schmalian, and I. R. Fisher, *Phys. Rev. B* **86**, 134507 (2012).
- ³⁵ M. M. Qazilbash, J. J. Hamlin, R. E. Baumbach, L. Zhang, D. J. Singh, M. B. Maple, and D. N. Basov, *Nat. Phys.* **5**, 647 (2009).
- ³⁶ T. Sato, K. Nakayama, Y. Sekiba, P. Richard, Y. M. Xu, S. Souma, T. Takahashi, G. F. Chen, J. L. Luo, N. L. Wang, et al., *Phys. Rev. Lett.* **103**, 047002 (2009).
- ³⁷ T. Yoshida, I. Nishi, A. Fujimori, M. Yi, R. G. Moore, D. H. Lu, Z. X. Shen, K. Kihou, P. M. Shirage, H. Kito, et al., *J. Phys. Chem. Solids* **72**, 465 (2011).
- ³⁸ T. Yoshida, S.-I. Ideta, I. Nishi, A. Fujimori, M. Yi, R. G. Moore, S.-K. Mo, D. Lu, Z.-X. Shen, Z. Hussain, et al., *Front. Phys.* **2**, 17 (2014).
- ³⁹ A. I. Coldea, J. D. Fletcher, A. Carrington, J. G. Analytis, A. F. Bangura, J. H. Chu, A. S. Erickson, I. R. Fisher, N. E. Hussey, and R. D. McDonald, *Phys. Rev. Lett.* **101**, 216402 (2008).
- ⁴⁰ T. Terashima, M. Kimata, N. Kurita, H. Satsukawa, A. Harada, K. Hazama, M. Imai, A. Sato, K. Kihou, C.-H. Lee, et al., *J. Phys. Soc. Jpn.* **79**, 3702 (2010).
- ⁴¹ A. Carrington, *Reports on Progress in Physics* **74**, 124507 (2011).
- ⁴² C. Putzke, A. I. Coldea, I. Guillamn, D. Vignolles, A. McCollam, D. Leboeuf, M. D. Watson, I. I. Mazin, S. Kasahara, T. Terashima, et al., *Phys. Rev. Lett.* **108**, 047002 (2012).
- ⁴³ T. Terashima, N. Kurita, M. Kimata, M. Tomita, S. Tsuchiya, M. Imai, A. Sato, K. Kihou, C.-H. Lee, H. Kito, et al., *Phys. Rev. B* **87**, 224512 (2013).
- ⁴⁴ F. Hardy, A. E. Böhmer, D. Aoki, P. Burger, T. Wolf, P. Schweiss, R. Heid, P. Adelmann, Y. X. Yao, G. Kotliar, et al., *Phys. Rev. Lett.* **111**, 027002 (2013).
- ⁴⁵ A. E. Böhmer, Ph.D. thesis, KIT Karlsruhe (2014).
- ⁴⁶ I. I. Mazin and M. D. Johannes, *Nat. Phys.* **5**, 141 (2009).
- ⁴⁷ Z. P. Yin, K. Haule, and G. Kotliar, *Nat. Mater.* **10**, 932 (2011).
- ⁴⁸ M. Aichhorn, S. Biermann, T. Miyake, A. Georges, and M. Imada, *Phys. Rev. B* **82**, 064504 (2010).
- ⁴⁹ P. Hansmann, R. Arita, A. Toschi, S. Sakai, G. Sangiovanni, and K. Held, *Phys. Rev. Lett.* **104**, 197002 (2010).
- ⁵⁰ M. Aichhorn, L. Pourovskii, and A. Georges, *Phys. Rev. B* **84**, 054529 (2011).
- ⁵¹ J. Ferber, K. Foyevtsova, R. Valentí, and H. O. Jeschke, *Phys. Rev. B* **85**, 094505 (2012).
- ⁵² J. Ferber, H. O. Jeschke, and R. Valentí, *Phys. Rev. Lett.* **109**, 236403 (2012).
- ⁵³ P. Werner, M. Casula, T. Miyake, F. Aryasetiawan, A. J. Millis, and S. Biermann, *Nat. Phys.* **8**, 331 (2012).
- ⁵⁴ K. Haule and G. Kotliar, *New J. Phys.* **11**, 025021 (2009).
- ⁵⁵ L. de' Medici, J. Mravlje, and A. Georges, *Phys. Rev. Lett.* **107**, 256401 (2011).
- ⁵⁶ R. Yu and Q. Si, *Phys. Rev. B* **84**, 235115 (2011).
- ⁵⁷ M. Aichhorn, L. Pourovskii, V. Vildosola, M. Ferrero, O. Parcollet, T. Miyake, A. Georges, and S. Biermann, *Phys. Rev. B* **80**, 085101 (2009).
- ⁵⁸ A. Liebsch, *Phys. Rev. B* **84**, 180505 (2011).
- ⁵⁹ A. Georges, L. de Medici, and J. Mravlje, *Annu. Rev. Condens. Matter Phys.* **4**, 137 (2013).
- ⁶⁰ Y. X. Yao, J. Schmalian, C. Z. Wang, K. M. Ho, and G. Kotliar, *Phys. Rev. B* **84**, 245112 (2011).
- ⁶¹ R. Yu and Q. Si, *Phys. Rev. Lett.* **110**, 146402 (2013).
- ⁶² L. de' Medici, G. Giovannetti, and M. Capone, *Phys. Rev. Lett.* **112**, 177001 (2014).
- ⁶³ L. Fanfarillo and E. Bascones, *Phys. Rev. B* **92**, 075136 (2015).
- ⁶⁴ F. F. Tafti, A. Juneau-Fecteau, M. Delage, S. Ren de Cotret, J. P. Reid, A. F. Wang, X. G. Luo, X. H. Chen, N. Doiron-Leyraud, and L. Taillefer, *Nat. Phys.* **9**, 349 (2013).
- ⁶⁵ K. Kihou, T. Saito, S. Ishida, M. Nakaajima, Y. Tomioka, H. Fukazawa, Y. Kohori, T. Ito, S.-i. Uchida, A. Iyo, et al., *J. Phys. Soc. Jpn.* **79**, 4713 (2010).
- ⁶⁶ J. K. Dong, S. Y. Zhou, T. Y. Guan, H. Zhang, Y. F. Dai, X. Qiu, X. F. Wang, Y. He, X. H. Chen, and S. Y. Li, *Phys. Rev. Lett.* **104**, 087005 (2010).
- ⁶⁷ F. Eilers, Ph.D. thesis, KIT Karlsruhe (2014).
- ⁶⁸ Z. Zhang, A. F. Wang, X. C. Hong, J. Zhang, B. Y. Pan, J. Pan, Y. Xu, X. G. Luo, X. H. Chen, and S. Y. Li, *Phys. Rev. B* **91**, 024502 (2015).
- ⁶⁹ X. C. Hong, X. L. Li, B. Y. Pan, L. P. He, A. F. Wang, X. G. Luo, X. H. Chen, and S. Y. Li, *Phys. Rev. B* **87**, 144502 (2013).
- ⁷⁰ Y. Liu and T. A. Lograsso, *Phys. Rev. B* **90**, 224508 (2014).
- ⁷¹ P. Popovich, A. V. Boris, O. V. Dolgov, A. A. Golubov, D. L. Sun, C. T. Lin, R. K. Kremer, and B. Keimer, *Phys. Rev. Lett.* **105**, 027003 (2010).
- ⁷² G. Mu, H. Luo, Z. Wang, L. Shan, C. Ren, and H.-H. Wen, *Phys. Rev. B* **79**, 174501 (2009).
- ⁷³ S. L. Skornyakov, V. I. Anisimov, and D. Vollhardt, *Sov. Phys. J. Exp. Theor. Phys. Lett.* **100**, 120 (2014).
- ⁷⁴ J. G. Storey, J. W. Loram, J. R. Cooper, Z. Bukowski, and J. Karpinski, *Phys. Rev. B* **88**, 144502 (2013).
- ⁷⁵ Z. Shermadini, J. Kanter, C. Baines, M. Bendele, Z. Bukowski, R. Khasanov, H. H. Klauss, H. Luetkens, H. Maeter, G. Pascua, et al., *Phys. Rev. B* **82**, 144527 (2010).
- ⁷⁶ I. I. Mazin, D. J. Singh, M. D. Johannes, and M. H. Du, *Phys. Rev. Lett.* **101**, 057003 (2008).
- ⁷⁷ P. J. Hirschfeld, M. M. Korshunov, and I. I. Mazin, *Rep. Prog. Phys.* **74**, 124508 (2011).
- ⁷⁸ D. J. Scalapino, *Rev. Mod. Phys.* **84**, 1383 (2012).
- ⁷⁹ E. Dagotto, *Rev. Mod. Phys.* **85**, 849 (2013).
- ⁸⁰ T. Shibauchi, A. Carrington, and Y. Matsuda, *Annual Review of Condensed Matter Physics* **5**, 113 (2014).
- ⁸¹ H. Hosono and K. Kuroki, *Physica C* **514**, 399 (2015).
- ⁸² K. Koepernik and H. Eschrig, *Phys. Rev. B* **59**, 1743 (1999).
- ⁸³ J. P. Perdew, K. Burke, and M. Ernzerhof, *Phys. Rev. Lett.* **77**, 3865 (1996).
- ⁸⁴ P. Blaha, K. Schwarz, G. K. H. Madsen, D. Kvasnicka, and J. Luitz, *WIEN2k, An Augmented Plane Wave Plus Local Orbitals Program for Calculating Crystal Properties* (Karlheinz Schwarz, Techn. Universität Wien, Austria, 2001).

- ⁸⁵ G. Kresse and J. Hafner, *Phys. Rev. B* **47**, 558 (1993).
- ⁸⁶ G. Kresse and J. Furthmüller, *Comput. Mater. Sci.* **6**, 15 (1996).
- ⁸⁷ P. E. Blöchl, *Phys. Rev. B* **50**, 17953 (1994).
- ⁸⁸ E. Bitzek, P. Koskinen, F. Ghler, M. Moseler, and P. Gumbsch, *Phys. Rev. Lett.* **97**, 170201 (2006).
- ⁸⁹ M. Tomić, H. O. Jeschke, R. M. Fernandes, and R. Valentí, *Phys. Rev. B* **87**, 174503 (2013).
- ⁹⁰ W. Metzner and D. Vollhardt, *Phys. Rev. Lett.* **62**, 324 (1989).
- ⁹¹ E. Müller-Hartmann, *Zeitschrift für Physik B Condensed Matter* **76**, 211 (1989).
- ⁹² W. K. Antoine Georges, Gabriel Kotliar and M. J. Rozenberg, *Rev. Mod. Phys.* **68**, 13 (1996).
- ⁹³ S. Backes, D. Guterding, H. O. Jeschke, and R. Valentí, *New J. Phys.* **16**, 083025 (2014).
- ⁹⁴ P. Werner, A. Comanac, L. de' Medici, M. Troyer, and A. J. Millis, *Phys. Rev. Lett.* **97**, 076405 (2006).
- ⁹⁵ B. Bauer, L. D. Carr, H. G. Evertz, A. Feiguin, J. Freire, S. Fuchs, L. Gamper, J. Gukelberger, E. Gull, S. Guertler, et al., *Journal of Statistical Mechanics: Theory and Experiment* **2011**, P05001 (2011).
- ⁹⁶ E. Gull, Werner, S. Fuchs, B. Surer, T. Pruschke, and M. Troyer, *Comput. Phys. Commun.* **182**, 1078 (2011).
- ⁹⁷ J. Ferber, K. Foyevtsova, H. O. Jeschke, and R. Valentí, *Phys. Rev. B* **89**, 205106 (2014).
- ⁹⁸ A. I. Liechtenstein, V. I. Anisimov, and J. Zaanen, *Phys. Rev. B* **52**, R5467 (1995).
- ⁹⁹ K. S. D. Beach, arXiv:cond-mat/0403055 (unpublished).
- ¹⁰⁰ S. Graser, T. A. Maier, P. J. Hirschfeld, and D. J. Scalapino, *New J. Phys.* **11**, 025016 (2009).
- ¹⁰¹ A. Kreisel, Y. Wang, T. A. Maier, P. J. Hirschfeld, and D. J. Scalapino, *Phys. Rev. B* **88**, 094522 (2013).
- ¹⁰² M. Tomić, H. O. Jeschke, and R. Valentí, *Phys. Rev. B* **90**, 195121 (2014).
- ¹⁰³ M. Tomić, R. Valentí, and H. O. Jeschke, *Phys. Rev. B* **85**, 094105 (2012).
- ¹⁰⁴ N. Colonna, G. Profeta, A. Continenza, and S. Massidda, *Phys. Rev. B* **83**, 094529 (2011).
- ¹⁰⁵ Y.-Z. Zhang, H. C. Kandpal, I. Opahle, H. O. Jeschke, and R. Valentí, *Phys. Rev. B* **80**, 094530 (2009).
- ¹⁰⁶ J. E. Jörgensen and T. C. Hansen, *Eur. Phys. J. B* **78**, 411 (2010).
- ¹⁰⁷ S. Ran, S. L. Bud'ko, D. K. Pratt, A. Kreyssig, M. G. Kim, M. J. Kramer, D. H. Ryan, W. N. Rowan-Weetaluktuk, Y. Furukawa, B. Roy, et al., *Phys. Rev. B* **83**, 144517 (2011).
- ¹⁰⁸ S. Ran, S. L. Bud'ko, W. E. Straszheim, J. Soh, M. G. Kim, A. Kreyssig, A. I. Goldman, and P. C. Canfield, *Phys. Rev. B* **85**, 224528 (2012).
- ¹⁰⁹ E. Gati, S. Köhler, D. Guterding, B. Wolf, S. Knner, S. Ran, S. L. Bud'ko, P. C. Canfield, and M. Lang, *Phys. Rev. B* **86**, 220511 (2012).
- ¹¹⁰ R. S. Dhaka, R. Jiang, S. Ran, S. L. Bud'ko, P. C. Canfield, M. Tomić, R. Valentí, Y. Lee, B. N. Harmon, and A. Kaminski, *Phys. Rev. B* **89**, 020511(R) (2014).
- ¹¹¹ S. L. Bud'ko, X. Ma, M. Tomic, S. Ran, R. Valentí, and P. C. Canfield, *Phys. Rev. B* **93**, 024516 (2016).
- ¹¹² N. N. Greenwood and T. C. Gibb, *Mössbauer Spectroscopy* (Chapman and Hall Ltd, London, 1971).
- ¹¹³ S. Backes and H. O. Jeschke, *Phys. Rev. B* **88**, 075111 (2013).
- ¹¹⁴ E. C. Blomberg, M. A. Tanatar, A. Kreyssig, N. Ni, A. Thaler, R. Hu, S. L. Bud'ko, P. C. Canfield, A. I. Goldman, and R. Prozorov, *Phys. Rev. B* **83**, 134505 (2011).
- ¹¹⁵ A. Cano, M. Civelli, I. Eremin, and I. Paul, *Phys. Rev. B* **82**, 020408 (2010).
- ¹¹⁶ V. Barzykin and L. P. Gor'Kov, *Phys. Rev. B* **79**, 134510 (2009).
- ¹¹⁷ A. I. Coldea, private communication (2015).
- ¹¹⁸ G. Lee, H. S. Ji, Y. Kim, C. Kim, K. Haule, G. Kotliar, B. Lee, S. Khim, K. H. Kim, K. S. Kim, et al., *Phys. Rev. Lett.* **109**, 177001 (2012).
- ¹¹⁹ A. F. Kemper, T. A. Maier, S. Graser, H. P. Cheng, P. J. Hirschfeld, and D. J. Scalapino, *New J. Phys.* **12**, 073030 (2010).
- ¹²⁰ J. Diehl, S. Backes, D. Guterding, H. O. Jeschke, and R. Valentí, *Phys. Rev. B* **90**, 085110 (2014).
- ¹²¹ C. Liu, T. Kondo, N. Ni, A. D. Palczewski, A. Bostwick, G. D. Samolyuk, R. Khasanov, M. Shi, E. Rotenberg, S. L. Bud'ko, et al., *Phys. Rev. Lett.* **102**, 167004 (2009).
- ¹²² J. H. Soh, G. S. Tucker, D. K. Pratt, D. L. Abernathy, M. B. Stone, S. Ran, S. L. Bud'ko, P. C. Canfield, A. Kreyssig, R. J. McQueeney, et al., *Phys. Rev. Lett.* **111**, 227002 (2013).
- ¹²³ S. Backes, H. O. Jeschke, and R. Valentí, *Phys. Rev. B* **92**, 195128 (2015).
- ¹²⁴ F. F. Tafti, J. P. Clancy, M. Lapointe-Major, C. Collignon, S. Faucher, J. A. Sears, A. Juneau-Fecteau, N. Doiron-Leyraud, A. F. Wang, X. G. Luo, et al., *Phys. Rev. B* **89**, 134502 (2014).
- ¹²⁵ F. F. Tafti, A. Ouellet, A. Juneau-Fecteau, S. Faucher, M. Lapointe-Major, N. Doiron-Leyraud, A. F. Wang, X. G. Luo, X. H. Chen, and L. Taillefer, *Phys. Rev. B* **91**, 054511 (2015).
- ¹²⁶ J.-J. Ying, L.-Y. Tang, V. V. Struzhkin, H.-K. Mao, A. G. Gavriulik, A.-F. Wang, X.-H. Chen, and X.-J. Chen, arXiv:1501.00330 (unpublished).
- ¹²⁷ Y. Nakajima, R. Wang, T. Metz, X. Wang, L. Wang, H. Cynn, S. T. Wier, J. R. Jeffries, and J. Paglione, *Phys. Rev. B* **91**, 060508 (2015).
- ¹²⁸ D. Guterding, S. Backes, H. O. Jeschke, and R. Valentí, *Phys. Rev. B* **91**, 140503(R) (2015).
- ¹²⁹ R. Thomale, C. Platt, W. Hanke, J. Hu, and B. A. Bernevig, *Phys. Rev. Lett.* **107**, 117001 (2011).
- ¹³⁰ S. Maiti, M. M. Korshunov, T. A. Maier, P. J. Hirschfeld, and A. V. Chubukov, *Phys. Rev. Lett.* **107**, 147002 (2011).
- ¹³¹ S. Medvedev, T. M. McQueen, I. A. Troyan, T. Palasyuk, M. I. Erements, R. J. Cava, S. Naghavi, F. Casper, V. Ksenofontov, G. Wortmann, et al., *Nat. Mater.* **8**, 630 (2009).
- ¹³² J. K. Glasbrenner, I. I. Mazin, H. O. Jeschke, P. J. Hirschfeld, R. M. Fernandes, and R. Valentí, *Nature Physics* **11**, 953 (2015).
- ¹³³ J. Guo, S. Jin, G. Wang, S. Wang, K. Zhu, T. Zhou, M. He, and X. Chen, *Phys. Rev. B* **82**, 180520 (2010).
- ¹³⁴ E. W. Scheidt, V. R. Hathwar, D. Schmitz, A. Dunbar, W. Scherer, F. Mayr, V. Tsurkan, J. Deisenhofer, and A. Loidl, *Eur. Phys. J. B* **85**, 279 (2012).
- ¹³⁵ T. Noji, T. Hatakeda, S. Hosono, T. Kawamata, M. Kato, and Y. Koike, *Physica C* **504**, 8 (2014).
- ¹³⁶ S. Hosono, T. Noji, T. Hatakeda, T. Kawamata, M. Kato, and Y. Koike, *Journal of the Physical Society of Japan* **83**, 113704 (2014).
- ¹³⁷ S. J. Sedlmaier, S. J. Cassidy, R. G. Morris, M. Drakopoulos, C. Reinhard, S. J. Moorhouse, D. O'Hare, P. Manuel, D. Khalayavin, and S. J. Clarke, *J. Am. Chem. Soc.* **136**,

- 630 (2014).
- ¹³⁸ M. Burrard-Lucas, D. G. Free, S. J. Sedlmaier, J. D. Wright, S. J. Cassidy, Y. Hara, A. J. Corkett, T. Lancaster, P. J. Baker, S. J. Blundell, et al., *Nat. Mater.* **12**, 15 (2013).
- ¹³⁹ H. Sun, D. N. Woodruff, S. J. Cassidy, G. M. Allcroft, S. J. Sedlmaier, A. L. Thompson, P. A. Bingham, S. D. Forder, S. Cartenet, N. Mary, et al., *Inorganic Chemistry* **54**, 1958 (2015).
- ¹⁴⁰ T. P. Ying, X. L. Chen, G. Wang, S. F. Jin, T. T. Zhou, X. F. Lai, H. Zhang, and W. Y. Wang, *Sci. Rep.* **2**, 426 (2012).
- ¹⁴¹ A. Krzton-Maziopa, E. V. Pomjakushina, V. Y. Pomjakushin, F. von Rohr, A. Schilling, and K. Conder, *J. Phys.: Condens. Matter* **24**, 382202 (2012).
- ¹⁴² F.-C. Hsu, J.-Y. Luo, K.-W. Yeh, T.-K. Chen, T.-W. Huang, P. M. Wu, Y.-C. Lee, Y.-L. Huang, Y.-Y. Chu, D.-C. Yan, et al., *Proceedings of the National Academy of Sciences* **105**, 14262 (2008).
- ¹⁴³ K.-W. Yeh, T.-W. Huang, Y. lin Huang, T.-K. Chen, F.-C. Hsu, P. M. Wu, Y.-C. Lee, Y.-Y. Chu, C.-L. Chen, J.-Y. Luo, et al., *EPL (Europhysics Letters)* **84**, 37002 (2008).
- ¹⁴⁴ F. Wang, F. Yang, M. Gao, Z.-Y. Lu, T. Xiang, and D.-H. Lee, *Europhys. Lett.* **93**, 57003 (2011).
- ¹⁴⁵ A. Krzton-Maziopa, Z. Shermadini, E. Pomjakushina, V. Pomjakushin, M. Bendele, A. Amato, R. Khasanov, H. Luetkens, and K. Conder, *Journal of Physics: Condensed Matter* **23**, 052203 (2011).
- ¹⁴⁶ A. Zhang, T. Xia, K. Liu, W. Tong, Z. Yang, and Q. Zhang, *Scientific Reports* **3**, 1216 (2013).
- ¹⁴⁷ T. Ying, X. Chen, G. Wang, S. Jin, X. Lai, T. Zhou, H. Zhang, S. Shen, and W. Wang, *Journal of the American Chemical Society* **135**, 2951 (2013).
- ¹⁴⁸ L. Zheng, M. Izumi, Y. Sakai, R. Eguchi, H. Goto, Y. Takabayashi, T. Kambe, T. Onji, S. Araki, T. C. Kobayashi, et al., *Phys. Rev. B* **88**, 094521 (2013).
- ¹⁴⁹ J. Guo, H. Lei, F. Hayashi, and H. Hosono, *Nat. Commun.* **5**, 4756 (2014).
- ¹⁵⁰ X. F. Lu, N. Z. Wang, G. H. Zhang, X. G. Luo, Z. M. Ma, B. Lei, F. Q. Huang, and X. H. Chen, *Phys. Rev. B* **89**, 020507 (2014).
- ¹⁵¹ F. Hayashi, H. Lei, J. Guo, and H. Hosono, *Inorganic Chemistry* **54**, 3346 (2015).
- ¹⁵² S. Hosono, T. Noji, T. Hatakeda, T. Kawamata, M. Kato, and Y. Koike, *Journal of the Physical Society of Japan* **85**, 013702 (2016).
- ¹⁵³ D. Guterding, H. O. Jeschke, P. J. Hirschfeld, and R. Valentí, *Phys. Rev. B* **91**, 041112(R) (2015).
- ¹⁵⁴ K. V. Yusenko, J. Sottmann, H. Emerich, W. A. Crichton, L. Malavasi, and S. Margadonna, *Chem. Commun.* **51**, 7112 (2015).